



Comparative study on the oxygen reduction reaction electrocatalytic activities of iron phthalocyanines supported on reduced graphene oxide, mesoporous carbon vesicle, and ordered mesoporous carbon



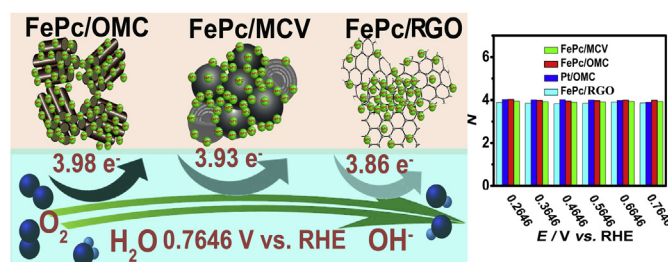
Mian Li, Xiangjie Bo*, Yufan Zhang, Ce Han, Liping Guo*

Faculty of Chemistry, Northeast Normal University, Changchun 130024, PR China

HIGHLIGHTS

- Novel FePc/carbon catalysts for ORR are fabricated by π – π stacking interactions.
- The FePc/OMC catalyst (FePc:OMC = 2:1) exhibits the best ORR catalytic activity.
- A positive correlation between ORR catalytic activity and specific surface area.
- Low H_2O_2 yield and 4e^- oxygen reduction process of FePc/OMC at low over potentials.
- Superior tolerance against methanol crossover and excellent stability of FePc/OMC.

GRAPHICAL ABSTRACT



ARTICLE INFO

Article history:

Received 14 January 2014

Received in revised form

16 April 2014

Accepted 17 April 2014

Available online 30 April 2014

Keywords:

Comparative study

Iron phthalocyanine

Reduced graphene oxide

Mesoporous carbon vesicle

Ordered mesoporous carbon

Oxygen reduction reaction

ABSTRACT

Iron phthalocyanine (FePc) is combined with different carbon matrixes (reduced graphene oxide (RGO), mesoporous carbon vesicle (MCV), and ordered mesoporous carbon (OMC)) through non-covalent π – π interaction. The nitrogen adsorption–desorption isotherms display that their specific surface areas obey an order of OMC > MCV > RGO. Raman spectroscopy reveals that OMC contains the most surface active sites. Meanwhile, SEM images show that the FePc monomers are more evenly dispersed on OMC than on MCV or RGO. Electrochemical measurements also display that oxygen reduction reaction (ORR) is catalyzed more easily on the FePc/OMC than on the FePc, FePc/MCV, and FePc/RGO, undoubtedly testifying the importances of specific surface area and surface active sites of OMC matrix for uniformly dispersing FePc molecules and then improving the ORR performances. Particularly, experiment results reveal that the FePc/OMC catalyst displays an enhanced 4-electron pathway in ORR either in acid or in alkaline media. Meanwhile, the FePc/OMC also shows better durability and superior stability towards methanol crossover than the Pt/OMC catalyst in both acid and alkaline media, potentially making the FePc/OMC a non-precious metal catalyst for ORR in fuel cells.

© 2014 Elsevier B.V. All rights reserved.

1. Introduction

Fuel cells (FCs) are clean, efficient, and dependable sources of energy and they are expected to become widely employed in the near future. It is well known that the oxygen reduction reaction

* Corresponding authors. Tel./fax: +86 0431 85099762.

E-mail addresses: baoxj133@nenu.edu.cn (X. Bo), guolp078@nenu.edu.cn (L. Guo).

(ORR) which takes place at the cathode is particularly important in FCs. However, the inherently poor efficiency and the sluggish reaction kinetics of the ORR have retarded the implementation of low-temperature FCs [1]. In regard to these problems, the ORR on noble metal surfaces such as Platinum (Pt) remains as one of the well-investigated electrochemical processes [2]. In spite of the outstanding performance of Pt-based ORR electro-catalysts, the commercialization is hampered by the high cost, the weak tolerance to methanol crosses, and the relatively poor durability of noble metal [3]. Thus, developing highly efficient and low-cost catalysts for ORR to reduce or replace Pt-based catalysts is a key step to the fabrication of commercially viable FC devices for future energy applications [4].

Since MN_4 -centers of transition-metals were firstly reported for catalyzing the ORR by R. Jasinski [5], numerous phthalocyanine and porphyrin-based materials have been widely investigated for the ORR [6,7]. Among them, iron phthalocyanine (FePc)-based materials hold the best performance (the electro-catalytic reduction of molecular oxygen occurs at a low over-potential) and they can be synthesized more easily. Regrettably, most FePc-based catalysts have not reached the level of Pt-based catalysts in terms of catalytic activity and stability [8,9]. From the previous literature, three main causes have confined the ORR performances of the FePc-based catalysts: (1) The relatively poor electrochemical stabilities of ORR on these catalysts. (2) The FePc molecules are prone to aggregation, which will greatly decrease the active sites for ORR. (3) The poor electron conductivity of the FePc molecules does not facilitate the electron transfer in the ORR process [10]. On the other hand, polymeric and heat-treated $M-N_4$ forms have been fabricated in order to obtain better stability, higher electronic conductivity, and more excellent ORR catalytic activity. Unfortunately, these methods indeed result in complex experiments and tailoring the structures and the surface properties of catalysts becomes difficult. To our best knowledge, the overall efficiency of a cathode is not only governed by the intrinsic activity of catalyst but also regulated by the active site density. It has been considered that the type of support material (to which the metal phthalocyanine is attached) has a significant effect on the promotion of electro-catalytic activity and durability. To design more effective catalytic systems for ORR, FePc has been studied by supporting it on some carbon materials. Vulcan XC-72 carbon black containing good compromise between electronic conductivity and specific surface area has been used as support material for attaching FePc molecules [11]. Recently, carbon nanotube and graphene have also been demonstrated as catalyst supports for FePc molecules [6,12]. However, it is hard to uniformly disperse FePc molecules on these carbon matrixes because of their restricted superficial areas and active sites, certainly leading to the poor ORR catalytic activities when compared with the Pt-based catalysts. Hence, improving ORR performances of FePc-based materials still needs to be explored.

Since the ordered mesoporous carbon (OMC) was synthesized in 1999 [13], intensive attentions have been paid on the electrochemical applications of OMC because of its uniform and tailored pore structure (which will afford more surface active sites), high specific surface area, large pore volume, and good electrical conduction ability [14–17]. The Onion-like mesoporous carbon vesicle (MCV) is another kind of mesoporous carbon material containing specific multilayer lamellar structure, considerable specific surface area, and large pore volume [18]. The two kinds of ordered mesoporous materials have already been used as supports for some catalytic centers (such as: Pt, Ni, Cu_2O , glucose oxidases, etc.) and the prepared compounds show excellent catalytic activities [14,17,19]. However, to the best of our knowledge, no attempt has been made to synthesize FePc/OMC or FePc/MCV composites for ORR. The dispersive status of the FePc molecules on OMC and MCV

and the ORR electro-catalytic activities of the FePc/OMC and FePc/MCV catalysts are almost completely unknown. Reduced graphene oxide (RGO) is well known as its unique 2D structure and extraordinary electronic property. As far as we are aware, although the RGO has been studied as the matrix for supporting the FePc molecules, it is still unknown whether the ORR catalytic activity of the FePc/RGO catalyst is comparable to those of FePc/porous carbon materials. Thus, it has motivated our curiosity to explore the relationships of the ORR catalytic activities of the FePc/carbon catalysts to their carbon matrixes and then develop efficient non-noble metal catalysts for the ORR.

In this paper, the FePc monomers were immobilized onto different carbon matrixes (RGO, MCV, and OMC) through π – π interaction. A comparative study on the ORR electro-catalytic activities of the FePc/RGO, FePc/MCV, and FePc/OMC catalysts is reported for the first time. To understand the relationships between the structures of carbon matrixes and the ORR catalytic activities, the structure characterizations were investigated by scanning electron spectroscopy (SEM), transmission electron microscopy (TEM), nitrogen adsorption–desorption isotherm, Raman Spectroscopy, X-ray diffraction (XRD), and Fourier transform infrared spectroscopy (FT-IR). The ORR catalytic activities of the FePc/RGO, FePc/MCV, FePc/OMC, and Pt/OMC catalysts were also studied by cyclic voltammetry (CV), rotating disk electrode (RDE), and rotating ring-disk electrode (RRDE) measurements, respectively.

2. Experimental

2.1. Materials and reagents

Pluronic P123 (non-ionic triblock copolymer, $EO_{20}PO_{70}EO_{20}$), Pluronic F127 (non-ionic triblock copolymer, $PEO_{106}PPO_{70}PEO_{106}$), tetraethyl orthosilicate (TEOS), Nafion (5 wt% solution), methanol, hydrazine, and N,N-Dimethylformamide (DMF) were purchased from Sinopharm Chemical Reagent Co., Ltd. The FePc (purity: 96%) was purchased from Alfa Aesar (Ward Hill, MA, USA). All other chemicals were of analytical reagent grade and used as received. Highly purified nitrogen ($\geq 99.99\%$) and oxygen ($\geq 99.99\%$) were supplied by Changchun Juyang Co Ltd. Ultrapure water (resistivity: $\rho \geq 18 \text{ M}\Omega \text{ cm}^{-1}$) was used to prepare the solutions.

2.2. Catalyst synthesis and preparation of modified electrode

The mesoporous Santa Barbara Amorphous No.15 (SBA-15) was synthesized using TEOS as silica source and Pluronic P123 as surfactant. OMC was synthesized by using SBA-15 as template and sucrose as carbon source according to the method reported previously [13]. Onion-like MCV was prepared according to the method reported by Zhao et al. [18]. GO was synthesized from graphite powder by using Hummer's method [20]. RGO was obtained by chemically reducing the GO powders with hydrazine. Briefly, 10 mg of GO was dispersed in 15 mL of distilled water by ultrasound for 4 h, and hydrazine monohydrate (5 mL) was subsequently added into the dispersion. The chemical reaction was allowed to proceed under stirring and heating at 80°C overnight. The reaction products were washed with distilled water on a sintered glass filter (medium pore size), and dried under vacuum at 80°C . To prepare FePc/OMC catalyst, 10 mg of the as-synthesized OMC was firstly dispersed in 20 mL of DMF with 30 min of ultrasonication, then 20 mg of FePc was added into the prepared OMC/DMF suspension. After 30 min of ultrasonication, the suspension was vehemently stirred for another 48 h at room temperature. Subsequently, the resulting solution was adequately centrifuged to get the precipitates. For the optimization, a series of FePc/OMC compounds containing different mass ratios of FePc and OMC were prepared by the same procedure

(FePc/OMC = 3:1, 2:1, 1:1, and 1:2 w/w, respectively). Meanwhile for comparison, FePc/MCV and FePc/RGO (FePc:carbon matrix = 2:1) were also prepared by using the same procedure. In addition, Pt/OMC catalyst (containing 20 wt% of Pt) was prepared by ethylene glycol reduction method with the microwave-assist [21].

A glassy carbon electrode (GCE, $d = 5$ mm) was used as RDE in electrochemical experiments. Prior to be modified, it was polished carefully with 1.00, 0.30, and 0.05 μm alumina powders and then cleaned with HNO_3 (1:1), ethanol, and deionized water, respectively. Catalyst ink was prepared by mixing 3 mg of the prepared catalyst powders into 1 mL of Nafion solution (0.1 wt%) with 45 min of ultrasonication. Then 14 μL of the catalyst ink was dropped onto the clean-washed GCE and dried under an infrared lamp before electrochemical experiments.

2.3. Physical characterizations

Philips XL-30 ESEM was used to determine the morphology of catalyst. The TEM images were obtained using a JEM-2100F transmission electron microscope (JEOL, Japan) operating at 200 kV. The nitrogen adsorption–desorption isotherms were performed on an ASAP 2020 (Micromeritics, USA). Before the measurements, samples were degassed in vacuum at 120 $^\circ\text{C}$ for 6 h. The Brunauer–Emmett–Teller (BET) method was utilized to calculate the specific surface areas by using adsorption data. The pore size distribution was derived from the adsorption branches by using the Barrett–Joyner–Halenda (BJH) model. The total pore volume (V_t) was estimated from the adsorbed amounts at a relative pressure (P/P_0) of ca.1. The surface chemistry of catalyst was analyzed by using Raman spectroscopy (HR800, Jobin Yvon). The FT-IR spectra of samples were recorded with Nicolet Magna 560 FT-IR spectrometer with a KBr plate. The XRD patterns were obtained on an X-ray D/max-2200vpc (Rigaku Corporation, Japan) instrument operated at 40 kV and 20 mA using Cu K radiation ($k = 0.15406$ nm).

2.4. Electrochemical measurements

To characterize the electrochemical properties of catalysts, we performed CV, RDE, and RRDE measurements using a three-electrode electrochemical cell (in which a modified RDE, an Ag/

AgCl (in saturated KCl solution), and a platinum wire served as the working, reference, and counter electrodes, respectively). CV curves were recorded by a CHI 660C electrochemical workstation (CH Instruments, China). Meanwhile, a speed control unit–Princeton Applied Research Model 636 Electrode Rotator and a Pine RRDE with GC disk and Pt ring were also used for RDE and RRDE measurements. All potentials appeared in this paper are referred to reversible hydrogen electrode (the potentials recorded and referred to Ag/AgCl in each experiment were calculated using the formula $E_{\text{RHE}} = E_{\text{Ag/AgCl}} + 0.059 \text{ pH} + 0.198 \text{ V}$, where E_{RHE} is a potential vs. reversible hydrogen electrode (RHE), $E_{\text{Ag/AgCl}}$ is a potential vs. Ag/AgCl electrode, and pH is the pH value of electrolyte [22,23]). All current densities are the ratios of currents and geometric areas of working electrodes.

3. Results and discussion

3.1. Physical characterizations of catalysts

The morphologies of the RGO, MCV, and OMC are firstly examined by SEM and TEM. Fig. 1A and B shows the typical SEM and TEM images of RGO sheets, it is clear that RGO exhibits representative laminated nanosheet structure. The SEM image of MCV (Fig. 1C) reveals that it is consisted of irregular spheres containing the particle sizes in a range of 100–250 nm. The detailed structure of MCV is exhibited by the TEM image in Fig. 1D. One can see that most spheres have the multilayer vesicle mesostructure and the distances between two layers vary from several nanometers to 24 nm, which indicates the good structural ordering of MCV. The morphology of OMC is displayed by the SEM image (Fig. 1E), which proves that OMC is made up of carbon nanorods. The typical TEM images viewed from the $[1\ 0\ 0]$ (Fig. 1F) and $[0\ 0\ 1]$ (the inset of Fig. 1F) directions for OMC provide direct visualization of the morphology and internal mesostructure of OMC, demonstrating that OMC exhibits highly ordered 2D-hexagonal arrays of carbon nanorods and well-developed mesoporous between adjacent carbon nanorods.

Fig. S1A presents the nitrogen adsorption–desorption isotherms of the RGO, MCV, and OMC. The N_2 -adsorption isotherms all exhibit type IV isotherms, indicating that these catalysts are porous. Fig. S1B

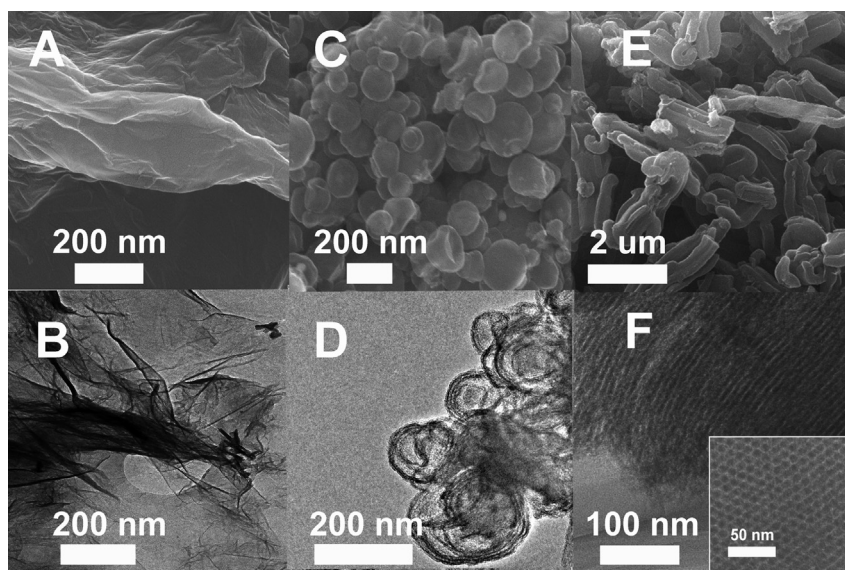


Fig. 1. SEM images of the RGO (A), MCV (C), and OMC (E). TEM images of the RGO (B), MCV (D), and OMC viewed from the $[1\ 0\ 0]$ (F) and $[0\ 0\ 1]$ (G) directions. (H) Nitrogen adsorption–desorption isotherms of the RGO (blue line), MCV (red line), and OMC (black line). (I) Pore size distributions for the RGO, MCV, and OMC, respectively.

reveals the pore-size distributions of the RGO, MCV, and OMC. One can see that the RGO has a pore-size distribution between 20 and 160 nm. However, the OMC and MCV contain the mean pore-size distributions of 6.7 and 4.8 nm (as shown in Fig. S1B) respectively, indicating that the ordered mesoporous structures are well-displayed for OMC and MCV. The textural properties of the RGO, MCV, and OMC are recorded in Table 1. It is clear that the OMC owns a BET surface area of $889.4 \text{ m}^2 \text{ g}^{-1}$ with a total pore volume of $1.6 \text{ cm}^3 \text{ g}^{-1}$, which are larger than those of the MCV ($793.6 \text{ m}^2 \text{ g}^{-1}$, $1.2 \text{ cm}^3 \text{ g}^{-1}$) and RGO ($118.5 \text{ m}^2 \text{ g}^{-1}$, $0.3 \text{ cm}^3 \text{ g}^{-1}$).

Fig. 2A–C shows the SEM images of the FePc/RGO, FePc/MCV, and FePc/OMC catalysts with a mass ratio of 2:1 (FePc: carbon). It could be observed that most FePc particles are located at the contact parts of different RGO layers (Fig. 2A). Astoundingly, most shells of MCV in the FePc/MCV compounds collapse (Fig. 2B) after they are vehemently stirred for 48 h, demonstrating the existence of multilayer vesicle mesostructure of MCV. Meanwhile, most FePc molecules are located between different carbon spheres. For the FePc/OMC (FePc:OMC = 2:1, Fig. 2C), the FePc molecules are evenly dispersed on the surface of OMC. However, the SEM image of FePc/OMC (FePc:OMC = 3:1, Fig. 2D) shows that the superabundant FePc molecules will repeatedly stack on the surface of OMC. The inset of Fig. 2D displays the structure of the FePc monomer, it is clear that the FePc molecule has a diameter of about 50 nm, and its length is between 30 and 100 nm.

As shown in Fig. 3A–C, the FT-IR spectrum of the FePc displays the representative peaks at 1506, 1415, 1329, 1285, 1161, 1117, 1079, and 719 cm^{-1} [24]. The FT-IR spectrum of RGO indicates the presences of C–O at 1065 cm^{-1} , C–O–C at 1225 cm^{-1} , C–O–H at 1400 cm^{-1} , C=C at 1620 cm^{-1} , and C=O at 1740 cm^{-1} [25]. However, The FT-IR spectra of the MCV (Fig. 3B) and OMC (Fig. 3C) samples only reveal weak O–H vermicular vibration (1185 cm^{-1}) and stretching vibration of C=C (1505 cm^{-1}) in benzenoid ring. The characteristic peaks of the FePc are still preserved in the FePc/RGO, FePc/MCV, and FePc/OMC compounds, but they all appear with slight shifts, indicating the formations of the π – π bonded FePc/carbon composites [26]. Thus, the formations of such non-covalent hybridizations of carbon matrixes conjugated by FePc molecules are hypothesized and verified by FT-IR spectra.

The XRD analyses were performed to characterize the structures of FePc/carbon composites. As shown in Fig. 3D–F, the sharp XRD peaks at $2\theta = 6.75^\circ$, 15.53° , and 24.68° are characteristic peaks of the FePc molecules. The broad peaks at about 25° in the XRD patterns are corresponding to the (002) reflection of the RGO (Fig. 3D), MCV (Fig. 3E), and OMC (Fig. 3F) compounds. After being modified with FePc molecules, the characteristic peaks of the FePc molecules still appear in their XRD diffraction spectra, but the positions shift slightly, suggesting the occurrence of monomeric FePc attached to carbon crystals [26].

Raman spectroscopy is a powerful tool to characterize carbon-based materials and has been used for obtaining further information on the structures and topologies of the FePc, RGO, MCV, OMC, and FePc/carbon materials herein. As shown in Fig. 4A, the Raman spectrum of RGO displays two prominent peaks at 1355 and

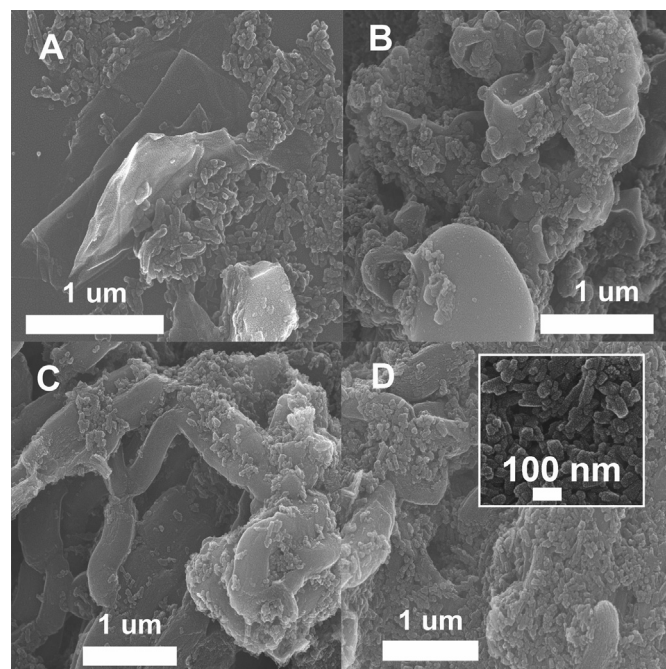


Fig. 2. SEM images of the FePc/RGO (A), FePc/MCV (B), and FePc/OMC (C) with the mass ratio (FePc: carbon matrix) of 1:1. (D) SEM image of FePc/OMC with the mass ratio (FePc: OMC) of 3:1, inset is SEM image of FePc.

1592 cm^{-1} , which corresponds to D and G bands respectively. The Raman spectra of the MCV (Fig. 4B) and OMC (Fig. 4C) also show both D and G bands at 1343, 1590 cm^{-1} and 1345, 1598 cm^{-1} , respectively. To our best knowledge, the D band is associated with structural defects and the G band is due to the E_{2g} vibration mode of sp^2 carbon domains [16]. Commonly, the relative intensity ratio of the D to G lines (I_D/I_G) is proportional to the number of defect sites in the carbon materials [27]. The increase of I_D/I_G from 1.44 for RGO to 1.74 for MCV and then to 1.93 for OMC (Fig. 4D) suggests that the OMC framework contains more edge plane-like defective sites than

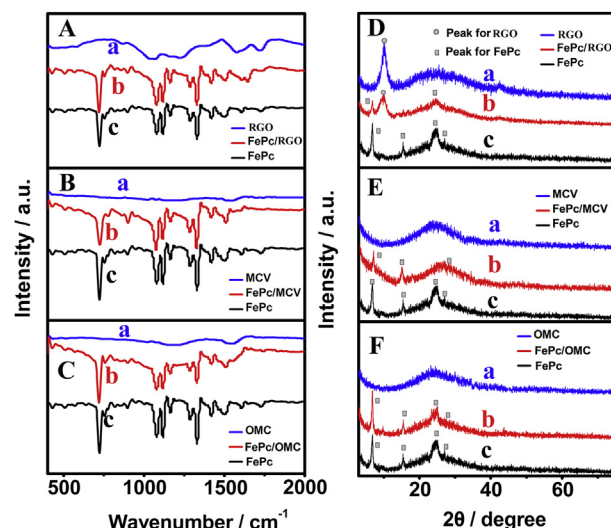


Fig. 3. (A) FT-IR spectra of the RGO (a), FePc/RGO (b), and FePc (c). (B) FT-IR spectra of the MCV (a), FePc/MCV (b), and FePc (c). (C) FT-IR spectra of the OMC (a), FePc/OMC (b), and FePc (c). (D) XRD patterns of the RGO (a), FePc/RGO (b), and FePc (c). (E) XRD patterns of the MCV (a), FePc/MCV (b), and FePc (c). (F) XRD patterns of the OMC (a), FePc/OMC (b), and FePc (c).

Table 1

Textural properties of OMC, MCV, and RGO.

Sample	$S_{\text{BET}}^a (\text{m}^2 \text{ g}^{-1})$	$S_{\text{E}}^b (\text{m}^2 \text{ g}^{-1})$	$V_{\text{t}}^c (\text{cm}^3 \text{ g}^{-1})$	$D^d (\text{nm})$
OMC	889.4	726.3	1.6	6.7
MCV	793.6	693.1	1.2	4.8
RGO	118.5	119.7	0.3	70.4

^a Total BET surface area.

^b External surface area.

^c Total pore volume.

^d Pore size.

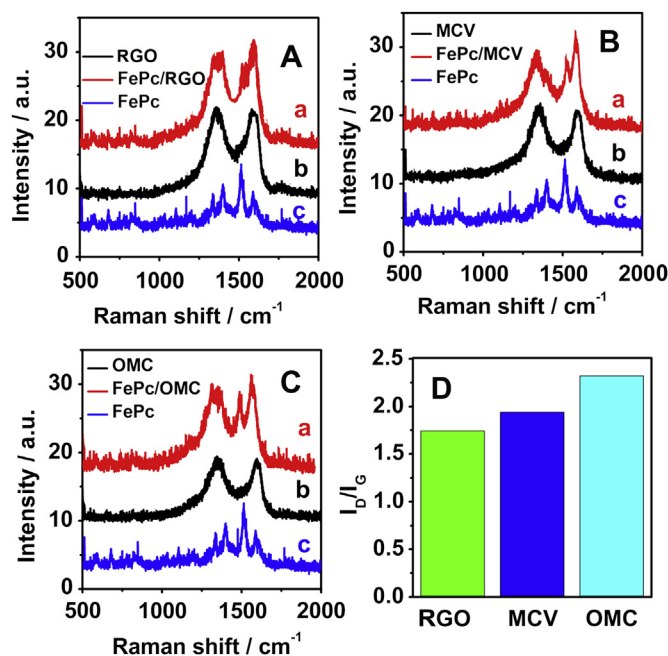


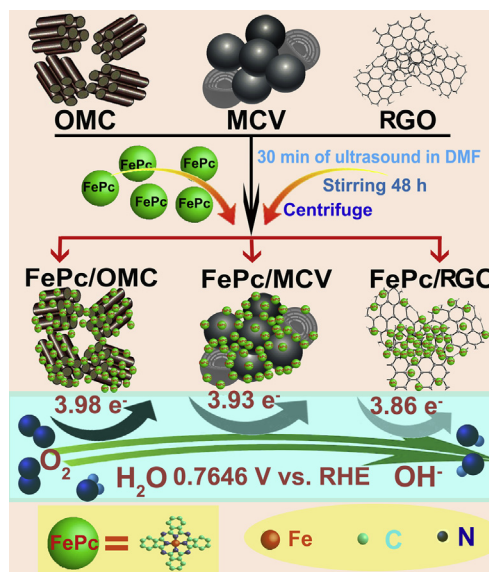
Fig. 4. (A) Raman spectra of the FePc/RGO (a), RGO (b), and FePc (c). (B) Raman spectra of the FePc/MCV (a), MCV (b), and FePc (c). (C) Raman spectra of the FePc/OMC (a), OMC (b), and FePc (c). (D) The I_D/I_G histograms of the RGO, MCV, and OMC.

the RGO and MCV, which is helpful to promote electron-transfer reactions and adsorb catalytic centers. After the modification of FePc molecules, most peaks for the FePc still appear in the spectra of the FePc/RGO, FePc/MCV, and FePc/OMC compounds. However, the I_D/I_G ratios of these FePc-based materials are lower than those of their corresponding carbon matrixes, demonstrating the larger average sp^2 domain sizes and lower defect site densities of these hybrid materials. Additionally, the positions of the D and G bands for the FePc/RGO, FePc/MCV, and FePc/OMC compounds all shift to lower wavenumbers. These shifts could be attributed to the π - π interaction between the FePc molecules and the carbon matrixes [6,26,28], consistent with the results acquired from the FT-IR and XRD tests.

The schematic interaction between the FePc molecules and the carbon matrixes and the ORR processes on the FePc/RGO, FePc/MCV, and FePc/OMC catalysts are illustrated in Scheme 1. The non-covalent binding is an optimal interaction without destroying the intrinsic properties of the FePc molecules and carbon matrixes. One can see that the OMC is a better selection to support FePc molecules with a high dispersion than the MCV and RGO because of its excellent specific surface area and abundant active sites. Meanwhile the FePc/OMC catalyst also shows more excellent ORR catalytic activity than those of FePc/MCV and FePc/RGO catalysts.

3.2. Catalytic activities of the FePc-based catalysts toward ORR

The catalytic activities of the FePc, FePc/RGO, FePc/MCV, and FePc/OMC catalysts to the ORR are firstly evaluated by using CV measurements performed in N_2 -saturated (Fig. 5A) and O_2 -saturated (Fig. 5B) 0.1 M KOH at a potential scan rate of 50 mV s^{-1} , respectively. As expected, no O_2 reduction activity is noted by the four samples in a N_2 -rich environment, but these catalysts all exhibit a pair of reversible redox peak centering on 0.865 V vs. RHE in the CV polarization curves, which is attributed to the redox reaction of $Fe(II)Pc/Fe(III)Pc$. Meanwhile, the background current densities for these catalysts decrease in an order of $FePc/OMC > FePc/MCV > FePc/RGO > FePc$, demonstrating the most active sites of the FePc/OMC compound.



Scheme 1. Illustration of the preparations of the FePc/RGO, FePc/MCV, and FePc/OMC as metal-free catalysts for ORR.

After the saturation of the solution with O_2 , distinct ORR responses are observed on all samples, suggesting their abilities to electrochemically catalyze ORR. For the FePc, the ORR peak potential (E_{peak}) is 0.753 V vs. RHE with a peak current density (j_{peak}) of $-0.619 \text{ mA cm}^{-2}$. Upon the load of the FePc molecules on carbon matrixes, the ORR E_{peak} positively shift to 0.787 V vs. RHE (FePc/RGO), 0.813 V vs. RHE (FePc/MCV), and 0.863 V vs. RHE (FePc/OMC) with the concomitant increase in j_{peak} to -1.457 (FePc/RGO), -2.219

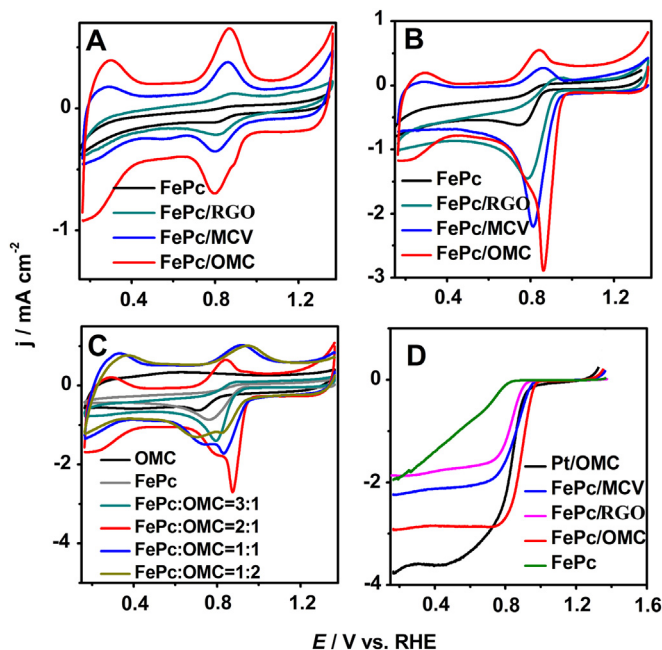


Fig. 5. CV curves of the FePc (black), FePc/RGO (dark cyan), FePc/MCV (blue), and FePc/OMC (red) in N_2 -saturated (A) and O_2 -saturated (B) 0.1 M KOH at a potential scan rate of 50 mV s^{-1} . (C) CV curves of the OMC, FePc, and FePc/OMC with different ingredients in O_2 -saturated 0.1 M KOH with a scan rate of 50 mV s^{-1} . (D) LSV curves of the Pt/OMC, FePc, and FePc/carbon materials in O_2 -saturated 0.1 M KOH at 5 mV s^{-1} , RDE rotating speed: 900 rpm. (For interpretation of the references to color in this figure legend, the reader is referred to the web version of this article.)

(FePc/MCV), and $-2.892 \text{ mA cm}^{-2}$ (FePc/OMC), respectively. These results clearly indicate the significant enhancement in ORR electrocatalytic activities of the FePc/RGO, FePc/OMC, and FePc/MCV catalysts compared with that of the FePc, undoubtedly highlighting the importance of carbon matrixes for enhancing ORR catalytic activity of the FePc molecules. Meanwhile, the CV test results also indicate that the excellent porous nature and the large specific surface area of the OMC matrix really act as the favorable factors for promoting the ORR performance of the FePc/OMC catalyst compared with FePc/MCV and FePc/RGO.

As shown in Fig. 5C, when the loading percentages of the FePc molecules change in the FePc/OMC catalysts, their ORR activities are also transformed obviously. The E_{peak} values are 0.711, 0.827, 0.833, 0.865, 0.796, and 0.753 V vs. RHE for the OMC, FePc/OMC (FePc:OMC = 1:2), FePc/OMC (FePc:OMC = 1:1), FePc/OMC (FePc:OMC = 2:1), FePc/OMC (FePc:OMC = 3:1), and FePc catalysts, respectively. Meanwhile, the j_{peak} values for them are -0.629 , -1.189 , -1.703 , -2.892 , -1.399 , and $-0.619 \text{ mA cm}^{-2}$, respectively. It is clear that a mass ratio of 2:1 (FePc: OMC) is the best choice for promoting the ORR catalytic activity of the FePc/OMC catalyst.

To further assess the ORR activities of these FePc-based catalysts, the linear sweep voltammetry (LSV) measurements were carried out in O_2 -saturated 0.1 M KOH solution at 5 mV s^{-1} . For comparison, the ORR performance of the Pt/OMC catalyst was also measured under the same condition. The LSV curves obtained at different electrodes with an electrode rotation rate of 900 rpm are shown in Fig. 5D. It can be seen that the FePc/RGO, FePc/MCV, and FePc/OMC catalysts have higher ORR catalytic activities than the FePc in terms of the onset potential (E_{onset}) and the half-wave potential ($E_{1/2}$). In particular, the FePc/OMC catalyst manifests the highest ORR catalytic activity accompanying more positive E_{onset} (0.950 V vs. RHE) and $E_{1/2}$ (0.892 V vs. RHE) than those of FePc/MCV (0.940 and 0.863 V vs. RHE), FePc/RGO (0.893 and 0.834 V vs. RHE), and FePc (0.848 and 0.569 V vs. RHE). Additionally, there is no obvious current platform appeared in the LSV curve of the FePc but the other three templated catalysts show high limiting current densities (j_L) at 0.400 V vs. RHE ($-2.875 \text{ mA cm}^{-2}$ for FePc/OMC, $-2.103 \text{ mA cm}^{-2}$ for FePc/MCV, and $-1.714 \text{ mA cm}^{-2}$ for FePc/RGO). In addition, although the j_L value of the FePc/OMC catalyst ($-2.875 \text{ mA cm}^{-2}$) is slightly lower than that of Pt/OMC ($-3.532 \text{ mA cm}^{-2}$), its E_{onset} (0.950 V vs. RHE) and $E_{1/2}$ (0.892 V vs.

RHE) are much more positive than those of Pt/OMC (0.885 and 0.801 V vs. RHE). Furthermore, the comparison of the E_{onset} value of the FePc/OMC catalyst with those of some other typical MPC (M = Fe, Co, or Ni)/carbon catalysts reported previously is given in Table S1. One can see that the FePc/OMC catalyst displays a more positive E_{onset} than most MPC/carbon catalysts, undoubtedly indicating a much higher intrinsic activity of the FePc/OMC as well as the importance of porous structure of the OMC matrix for enhancing the ORR catalytic activity of the FePc/carbon catalyst.

Selectivities of the 4-electron reduction of oxygen for the as-prepared FePc/carbon and Pt/OMC catalysts are further studied by using RDE technique. The LSV curves were recorded at different rotation rates from 100 to 2500 rpm in O_2 -saturated 0.1 M KOH solution at 5 mV s^{-1} as shown in Fig. 6A, C, E and G. The corresponding Koutecky–Levich (K–L) plots (j^{-1} vs. $\omega^{-1/2}$), shown in Fig. 6B, D, F and H) derived from the LSV curves according to the equations expressed as Eqs. (1) and (2) are used to assess the apparent numbers of electrons transferred during the ORR at various potentials [11,29]:

$$\frac{1}{j} = \frac{1}{j_k} + \frac{1}{j_L} \quad (1)$$

$$j_L = 0.62nFAD^{2/3}\nu^{-1/6}\omega^{1/2}C_{\text{O}_2} \quad (2)$$

where j , j_k , and j_L are the measured, kinetic, and diffusion limiting current densities (mA cm^{-2}), respectively; n is the number of electrons transferred during ORR and is extracted from the slope; F is the Faraday's constant ($96,485 \text{ C mol}^{-1}$); D is the diffusion coefficient of oxygen ($1.9 \times 10^{-5} \text{ cm}^2 \text{ s}^{-1}$); ν is the kinetic viscosity ($1.13 \times 10^{-2} \text{ cm}^2 \text{ s}^{-1}$); ω is the rotation rate of RDE (rpm); C_{O_2} is the bulk concentration of oxygen dissolved in the electrolyte ($1.2 \times 10^{-3} \text{ mol m}^{-3}$).

The linearity of the K–L plot and the near parallelism of the fitting lines suggest the first-order reaction kinetics toward the concentration of dissolved oxygen and a similar n value for the ORR at different potentials. Moreover, it is well known that the ORR catalyzed by Pt proceeds via a direct 4-electron pathway in alkaline media [30]. Therefore it is possible to gain a further understanding of the ORR pathway by the FePc/carbon and Pt/OMC catalysts through comparative K–L plots. The n values for the FePc/RGO, FePc/MCV, FePc/OMC, and Pt/OMC catalysts in the low over-

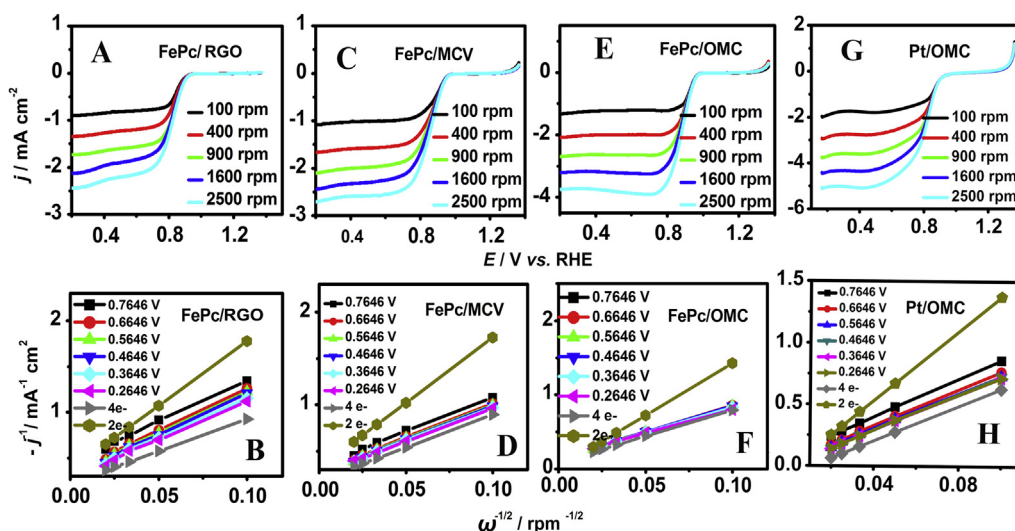


Fig. 6. LSV curves for the FePc/RGO (A), FePc/MCV (C), FePc/OMC (E), and Pt/OMC (G) in O_2 -saturated 0.1 M KOH at a potential scan rate of 5 mV s^{-1} ; RDE rotating speed changes from 100 rpm to 2500 rpm. The Koutecky–Levich (K–L) plots for the FePc/RGO (B), FePc/MCV (D), FePc/OMC (F), and Pt/OMC (H) at fixed potentials, respectively.

potential range (0.665–0.765 V vs. RHE) are ~ 3.85 , ~ 3.95 , ~ 4.01 , and ~ 3.99 , respectively (Fig. 7A). One can see that these n values are all close to 4. Particularly, the FePc/OMC catalyst exhibits a more dominant 4-electron oxygen reduction process in all potential range compared with the FePc/MCV and FePc/RGO compounds. At the same time, the n value of the FePc/MCV catalyst is similar to that of Pt/OMC.

To shed light on the origin of the synergistic effect and the intrinsic advantages of these FePc/carbon catalysts, the Tafel analyses were performed. The Tafel plots for these FePc-based catalysts all demonstrate two distinct linear regions at both low and high over-potentials (Fig. 7B). In the low over-potential region, where the overall ORR process is controlled by the kinetics of the surface reaction [31], the FePc/OMC compound gives a lower Tafel slope of $40.42 \text{ mV dec}^{-1}$ compared with the FePc/MCV ($46.45 \text{ mV dec}^{-1}$) and FePc/RGO ($53.65 \text{ mV dec}^{-1}$), likely provoked by facilitated electron transfer by OMC as well as its larger surface active area (which affords more active sites). However, in the high over-potential region, where the reaction speed is dominated by the

diffusion limitation inside the material, the Tafel slope of the FePc/OMC still yields the lowest value of $123.72 \text{ mV dec}^{-1}$, closely followed by the FePc/MCV ($148.82 \text{ mV dec}^{-1}$) and FePc/RGO ($163.65 \text{ mV dec}^{-1}$), revealing the apparently facilitated mass transfer inside OMC, which is better than MCV and RGO. It is clear that when other conditions are the same for these FePc-based catalysts except the carbon matrixes, the FePc/OMC shows the best ORR catalytic activity compared with the FePc/MCV and FePc/RGO. That is reasonably attributed to the unique pore architectures of the carbon micro blocks exposing the largest number of accessible active sites as well as the porous OMC serves as an electron channel enabling the rapid and sustainable reaction.

To continue verifying the ORR catalytic pathways of these FePc-based hybrid materials, we also performed the RRDE measurements to monitor the formation of peroxide species (H_2O_2) during the ORR process. The RRDE measurements were conducted in O_2 -saturated 0.1 M KOH at 5 mV s^{-1} with a rotation speed of 900 rpm, and the potential of the Pt ring electrode in the RRDE system was set as 1.500 V vs. RHE. Fig. 7C and D shows the disk and ring

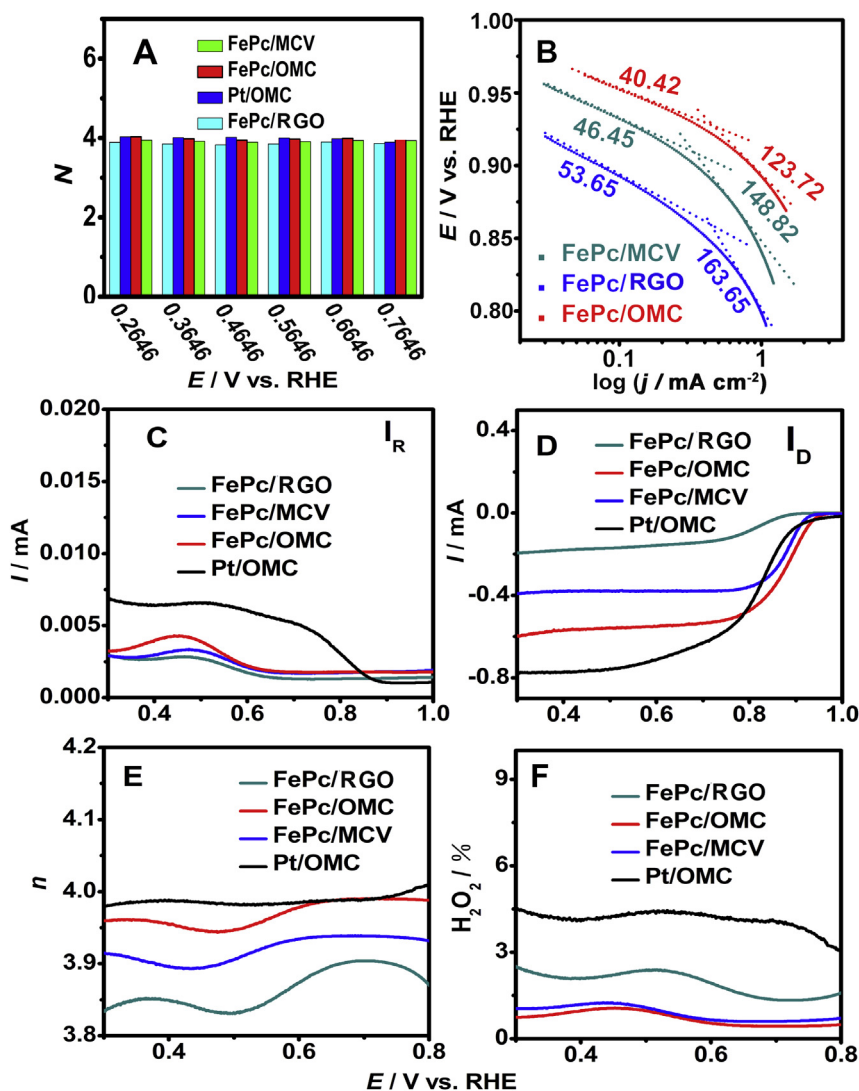


Fig. 7. (A) The dependences of n values on the potentials for the FePc/RGO, FePc/MCV, FePc/OMC, and Pt/OMC, respectively. (B) Tafel plots of the FePc/RGO, FePc/MCV, and FePc/OMC hybrid materials derived by the mass-transport correction of corresponding RDE data, respectively. The RRDE ring currents (C) and disk currents (D) of the FePc/RGO, FePc/MCV, FePc/OMC, and Pt/OMC, respectively. The RRDE measurements are carried out in O_2 -saturated 0.1 M KOH with an electrode rotating speed of 900 rpm. The ring potential of Pt ring is constant at 0.757 V vs. RHE. The electron transfer numbers (E) and percentages of peroxide (F) of different catalysts at various potentials are calculated from the corresponding RRDE data in (C) and (D).

currents for the FePc/RGO, FePc/MCV, FePc/OMC, and Pt/OMC catalysts. The n values can be calculated from the Eq. (3) and the percentage of H_2O_2 can be determined by Eq. (4) based on RRDE data recorded in Fig. 7C and D [31]:

$$n = \frac{4I_D}{(I_D + I_R/N)} \quad (3)$$

$$\% \text{H}_2\text{O}_2 = \frac{200I_R}{(I_D N + I_R)} \quad (4)$$

where N is the collection efficiency with a value of 0.37, I_D and I_R are the faradic-disk and -ring currents. Distinctly, over the low over-potential range (0.615–0.765 V vs. RHE), the FePc/OMC gives a n value of ~ 3.98 (Fig. 7E), and those for the FePc/MCV, FePc/RGO, and Pt/OMC catalysts are ~ 3.94 , ~ 3.88 , and ~ 3.98 , respectively. Meanwhile these results are consistent with the results obtained from the K–L plots based on the RDE measurements, suggesting that the FePc/OMC shows better catalytic activity than those of the FePc/MCV and FePc/RGO. In particular, the H_2O_2 yield of the FePc/OMC is less than 1% at all potentials and decreases to 0.5% at 0.765 V vs. RHE (Fig. 7F), which are lower than those of FePc/MCV (1.3%, 0.7%), FePc/RGO (2.4%, 1.4%), and Pt/OMC (4.5%, 3%). The CV, RDE, and RRDE measurements all verify that the FePc/OMC catalyst displays better ORR catalytic activity than those of FePc/MCV and FePc/RGO, undoubtedly indicating the excellent efficiency of OMC for promoting the ORR catalytic activity.

In view of the potential of the FePc/OMC catalyst as efficient ORR catalyst to replace the Pt-based ORR catalysts, we further tested the electrochemical stability and the possible methanol crossover in alkaline condition. The CV (Fig. S2A and B) and current–time (i – t) amperometric (Fig. S2C) test results prove that the FePc/OMC catalyst has higher selectivity toward the ORR and better methanol tolerance than those of Pt/OMC. The chronoamperometry (Fig. S2D) and potential cycling (Fig. S3) test results demonstrate that the FePc/OMC catalyst also holds better duration stability for ORR than that of Pt/OMC in alkaline medium.

In addition, the activity of the above optimal FePc/OMC in 0.5 M H_2SO_4 was also tested herein. As shown in Fig. 8A, the FePc/OMC catalyst displays a pronounced cathodic peak at about 0.493 V vs.

RHE with a j_{peak} value of $-0.872 \text{ mA cm}^{-2}$ in O_2 -saturated 0.5 M H_2SO_4 solution, suggesting that the FePc/OMC catalyst also shows the ORR catalytic activity in acidic condition. The RDE experiments were also performed to investigate the kinetics of electrochemical catalytic ORR at the FePc/OMC and Pt/OMC catalysts in 0.5 M H_2SO_4 solution, respectively. The comparison of LSVs obtained at the FePc/OMC and Pt/OMC catalysts with an electrode rotation rate of 900 rpm is shown in Fig. 8B. One can see that the j_L value of FePc/OMC ($-1.741 \text{ mA cm}^{-2}$) is lower than that of Pt/OMC ($-3.013 \text{ mA cm}^{-2}$). Meanwhile, its E_{onset} (0.725 V vs. RHE) and $E_{1/2}$ (0.623 V vs. RHE) are more negative than those of Pt/OMC (0.828 and 0.733 V vs. RHE). The LSV polarization curves recorded at different rotation rates are displayed in Fig. 8C and E. It is clear that the K–L plots of the FePc/OMC (Fig. 8D) and Pt/OMC (Fig. 8F) show good linearity with parallelism when the potential is below 0.450 V vs. RHE, which suggests a first-order dependence of O_2 kinetics on both electrodes. According to the K–L equations (Eqs. (1) and (2)), the n values for the FePc/OMC and Pt/OMC catalysts were calculated to be about 3.95 and 4.05, respectively, demonstrating that ORR on the FePc/OMC and Pt/OMC catalysts dominantly proceed with the 4-electron reaction pathways at a voltage range from 0.10 to 0.55 V vs. RHE.

The RRDE experiments were also implemented to characterize the electro-catalytic activities of the as-prepared FePc/OMC and Pt/OMC catalysts (Fig. 8G). The superior catalytic activity of the Pt/OMC over that of the FePc/OMC in acidic condition is also confirmed by the H_2O_2 yields (Fig. 8H) and n values (Fig. 8I) determined from the linear polarization curves. In particular, the numbers of electrons transferred are determined to be about 3.95 and 4.01 for the FePc/OMC and Pt/OMC catalysts with the peroxide yields of about 2.6% and 0.1% at 0.6 V vs. RHE. These results indicate that although the FePc/OMC and Pt/OMC catalysts show lower activity in acidic medium than in alkaline medium, they all remain the one-step and $4e^-$ transfer pathways.

The possible methanol crossovers and electrochemical stabilities of the FePc/OMC and Pt/OMC catalysts in acidic condition have also been tested. As shown in Fig. S4A, the characteristic peaks of ORR are maintained, no specific catalytic activity to methanol is observed on FePc/OMC, indicating that FePc/OMC can easily catalyze the reduction of O_2 and is tolerant to methanol in acidic

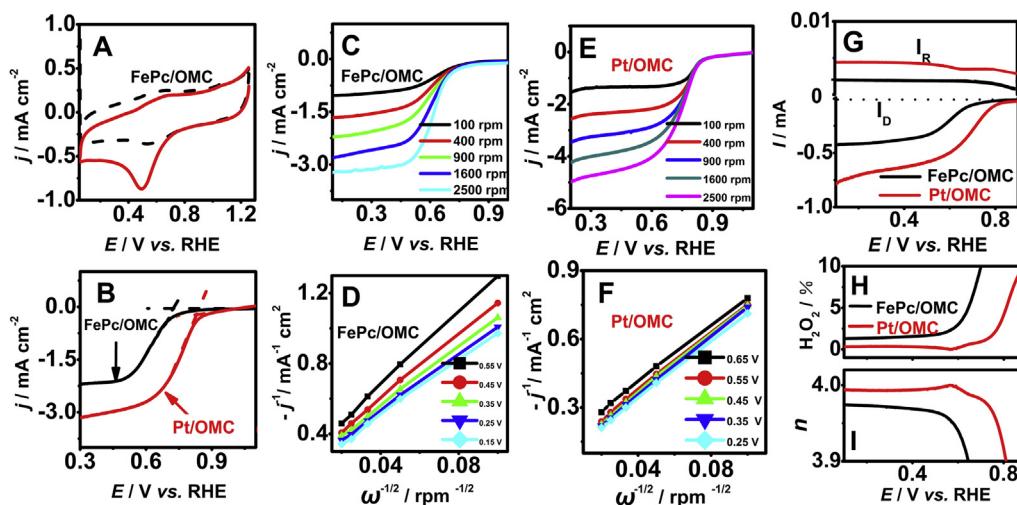


Fig. 8. (A) CV curves of the FePc/OMC in N_2 -saturated (black) and O_2 -saturated (red) 0.5 M H_2SO_4 at a potential scan rate of 50 mV s^{-1} . (B) LSV curves of the Pt/OMC and FePc/OMC at 5 mV s^{-1} , the RDE rotating speed is 900 rpm. LSV curves for the FePc/OMC (C) and Pt/OMC (E) at a potential scan rate of 5 mV s^{-1} ; RDE rotating speed changes from 100 rpm to 2500 rpm. The K–L plots for the FePc/OMC (D) and Pt/OMC (F) at fixed potentials, respectively. (G) The RRDE ring currents and disk currents of the FePc/OMC and Pt/OMC recorded with an electrode rotating speed of 900 rpm. The ring potential of Pt ring is constant at 0.757 V vs. RHE. The percentages of peroxide (H) and electron transfer numbers (I) of the FePc/OMC and Pt/OMC at various potentials are calculated from the corresponding RRDE data in (G). The RDE and RRDE tests are implemented in O_2 -saturated 0.5 M H_2SO_4 . (For interpretation of the references to color in this figure legend, the reader is referred to the web version of this article.)

condition. In contrast, the CV response for ORR on Pt/OMC shows a sharp decrease in current when in the presence of 3.0 M methanol (Fig. S4B), suggesting that the methanol oxidation reaction initiates. The chronoamperometry (Fig. S4C) and potential cycling (Fig. S5) measurement results demonstrate that the FePc/OMC catalyst holds better duration stability than Pt/OMC for the ORR in acidic medium. Finally, it is revealed that, based on our preliminary experiments, although the E_{onset} value of the FePc/OMC composite is slightly lower in acid media, its high durability and remarkable methanol tolerance either in alkaline solution or in acid media give it superiority over Pt/OMC and thus it can be used as non-precious metal cathodic catalyst for FCs.

4. Conclusions

We have designed novel FePc/carbon materials (carbon matrixes = RGO, MCV, and OMC) as the efficient non-precious metal catalysts for ORR. The SEM and TEM measurements clearly display the ordered mesoporous structure of the OMC. The nitrogen adsorption–desorption isotherms of these carbon matrixes also indicate that OMC has the largest BET surface area and total pore volume. Meanwhile, the Raman spectroscopy reveals that OMC contains the most surface active sites. The FT-IR, XRD, and Raman measurements reveal that the FePc/carbon materials are formed by non-covalent π – π stacking interaction between the carbon matrixes and the FePc molecules. Because of the excellent mesoporous structure (containing more active sites and larger surface area), FePc monomers are more evenly dispersed on the OMC than on the MCV or RGO. It is clear that the ORR is catalyzed more easily and efficiently on the FePc/OMC than on the FePc, FePc/MCV, and FePc/RGO catalysts. In particular, the FePc/OMC catalyst displays an enhanced 4-electron pathway in ORR either in acid or in alkaline media. Above all, experiment results reveal that FePc/OMC shows better durability and superior stability towards methanol crossover than Pt/OMC catalyst in both acid and alkaline media, potentially making the FePc/OMC a non-precious metal cathode catalyst for FCs.

Acknowledgments

The authors gratefully acknowledge the Research Fund for the Doctoral Program of Higher Education of China (20130043110006) and the Fundamental Research Funds for the Central Universities (No. 12SSXT145).

Appendix A. Supplementary data

Supplementary data related to this article can be found at <http://dx.doi.org/10.1016/j.jpowsour.2014.04.101>.

References

- [1] A. Mani, V.I. Birss, J. Electroanal. Chem. 687 (2012) 102–110.
- [2] A. Malika, E.B. Easton, J. Power Sources 236 (2013) 311–320.
- [3] D. Liu, X. Zhang, Z. Sun, T. You, Nanoscale 5 (2013) 9528–9531.
- [4] H. Zhu, S. Zhang, S. Guo, D. Su, S. Sun, J. Am. Chem. Soc. 135 (2013) 7130–7133.
- [5] R. Jasinski, Nature 201 (1964) 1212–1213.
- [6] C. Zhang, R. Hao, H. Yin, F. Liu, Y. Hou, Nanoscale 4 (2012) 7326–7329.
- [7] J. Jian, B. Xiangjie, W. Huan, Z. Yufan, L. Charles, G. Liping, Electrochem. Commun. 25 (2012) 35–38.
- [8] G. Dong, M. Huang, L. Guan, Phys. Chem. Chem. Phys. 14 (2012) 2557–2559.
- [9] T. Tasso, T. Furuyama, N. Kobayashi, Inorg. Chem. 52 (2013) 9206–9215.
- [10] J. Yuanyuan, L. Yizhong, L. Xiangyu, H. Dongxue, Z. Qixian, N. Li, C. Wei, ACS Catal. 3 (2013) 1263–1271.
- [11] M. Adina, C. Stéphane, F. Arianna, J. Bruno, P. Serge, Carbon 49 (2011) 4839–4847.
- [12] Y. Junbing, L. Di-Jia, N.K. Nancy, X.C. Lin, Chem. Commun. (2008) 329–331.
- [13] D. Zhao, J. Feng, Q. Huo, N. Melosh, G.H. Fredrickson, B.F. Chmelka, G.D. Stucky, Science 279 (1998) 548–552.
- [14] X. Bo, J. Bai, B. Qi, L. Guo, Biosens. Bioelectron. 28 (2011) 77–83.
- [15] B. Jing, N. Jean Chrysostome, L. Lin, Y. Li, G. Liping, J. Solid State Electrochem. 14 (2010) 2251–2256.
- [16] M. Zhou, J. Guo, L.-p. Guo, J. Bai, Anal. Chem. 80 (2008) 4642–4650.
- [17] Z. Yufan, B. Xiangjie, G. Liping, Anal. Methods 4 (2012) 736–741.
- [18] D. Gu, H. Bongard, Y. Deng, D. Feng, Z. Wu, Y. Fang, J. Mao, B. Tu, F. Schüth, D. Zhao, Adv. Mater. 22 (2010) 833–837.
- [19] Y. Xue, B. Xiangjie, G. Liping, Sens. Actuators B 155 (2011) 837–842.
- [20] W.S. Hummers, R.E. Offeman, J. Am. Chem. Soc. 80 (1958) 1339.
- [21] M. Li, X. Bo, Y. Zhang, C. Han, L. Guo, Biosens. Bioelectron. 56 (2014) 223–230.
- [22] H. Wang, X. Bo, Y. Zhang, L. Guo, Electrochem. Acta 108 (2013) 404–411.
- [23] W. Luo, Z. Yang, Z. Li, J. Zhang, J. Liu, Z. Zhao, Z. Wang, S. Yan, T. Yu, Z. Zou, Energy Environ. Sci. 4 (2011) 4046–4051.
- [24] S. Baranton, C. Coutanceau, C. Roux, F. Hahn, J.M. Léger, J. Electroanal. Chem. 577 (2005) 223–234.
- [25] H. Gao, F. Xiao, C. Ching, H. Duan, ACS Appl. Mat. Interfaces 3 (2011) 3049–3057.
- [26] M. Johannes Philipp, K. Teerakiat, S. Chakrit, W. Anurat, P. Ditsayut, L. Tanom, T. Adisorn, J. Mater. Chem. 22 (2012) 17094–17099.
- [27] L. Mian, B. Xiangjie, M. Zhongcheng, Z. Yufan, G. Liping, Sens. Actuators B 192 (2014) 261–268.
- [28] S. Wang, B. Goh, K. Manga, Q. Bao, P. Yang, K. Loh, ACS Nano 4 (2010) 6180–6186.
- [29] C. Lili, L. Guojun, D. Zhiyu, H. Xingquan, Electrochim. Acta 106 (2013) 272–278.
- [30] Y. Eunjo, Z. Haoshen, J. Power Sources 244 (2013) 429–434.
- [31] M. de Groot, M. Merckx, A. Wonders, M. Koper, J. Am. Chem. Soc. 127 (2005) 7579–7586.